Ruan D, Fessler J A and Balter J M 2008 Mean position tracking of respiratory motion *Med. Phys.* **35** 782–92
Schweikard A, Glosser G, Bodduluri M, Murphy M J and Adler J R 2000 Robotic motion compensation for respiratory
    movement during radiosurgery *Comput. Aided Surg.* **5** 263–77
Schweikard A, Shiomi H and Adler J 2004 Respiration tracking in radiosurgery *Med. Phys.* **31** 2738–41
Seppenwoolde Y, Berbeco R I, Nishioka S, Shirato H and Heijmen B 2007 Accuracy of tumor motion compensation
    algorithm from a robotic respiratory tracking system: a simulation study *Med. Phys.* **34** 2774–84
Seppenwoolde Y, Shirato H, Kitamura K, Shimizu S, van Herk M, Lebesque J V and Miyasaka K 2002 Precise and
    real-time measurement of 3D tumor motion in lung due to breathing and heartbeat, measured during radiotherapy
    Int. J. Radiat. Oncol. Biol. Phys. **53** 822–34
Shirato H *et al* 2000 Physical aspects of a real-time tumor-tracking system for gated radiotherapy *Int. J. Radiat.
    Oncol. Biol. Phys.* **48** 1187–95
Shirato H *et al* 2003 Feasibility of insertion/implantation of 2.0 mm diameter gold internal fiducial markers for
    precise setup and real-time tumor tracking in radiotherapy *Int. J. Radiat. Oncol. Biol. Phys.* **56** 240–7
Tsunashima Y, Sakae T, Shioyama Y, Kagei K, Terunuma T, Nohtomi A and Akine Y 2004 Correlation between the
    respiratory waveform measured using a respiratory sensor and 3D tumor motion in gated radiotherapy *Int. J.
    Radiat. Oncol. Biol. Phys.* **60** 951–8
Vedam S S, Kini V R, Keall P J, Ramakrishnan V, Mostafavi H and Mohan R 2003 Quantifying the predictability of
    diaphragm motion during respiration with a noninvasive external marker *Med. Phys.* **30** 505–13
Wade O L 1954 Movement of the thoracic cage and diaphragm in respiration *J. Physiol.* 193–212

A margin model to account for respiration-induced tumour motion and its variability

Catherine Coolens[1], Steve Webb[1], H Shirato[2], K Nishioka[2] and Phil M Evans[1]

[1] Joint Department of Physics, Institute of Cancer Research and Royal Marsden NHS Foundation Trust, Downs Road, Sutton, Surrey SM2 5PT, UK
[2] Department of Radiology, Hokkaido University Graduate School of Medicine, Sapporo, Japan

E-mail: Catherine.coolens@rmp.uhn.on.ca

Abstract

In order to reduce the sensitivity of radiotherapy treatments to organ motion, compensation methods are being investigated such as gating of treatment delivery, tracking of tumour position, 4D scanning and planning of the treatment, etc. An outstanding problem that would occur with all these methods is the assumption that breathing motion is reproducible throughout the planning and delivery process of treatment. This is obviously not a realistic assumption and is one that will introduce errors. A *dynamic internal margin model* (DIM) is presented that is designed to follow the tumour trajectory and account for the variability in respiratory motion. The model statistically describes the variation of the breathing cycle over time, i.e. the uncertainty in motion amplitude and phase reproducibility, in a polar coordinate system from which margins can be derived. This allows accounting for an additional gating window parameter for gated treatment delivery as well as minimizing the area of normal tissue irradiated. The model was illustrated with abdominal motion for a patient with liver cancer and tested with internal 3D lung tumour trajectories. The results confirm that the respiratory phases around exhale are most reproducible and have the smallest variation in motion amplitude and phase (approximately 2 mm). More importantly, the margin area covering normal tissue is significantly reduced by using trajectory-specific margins (as opposed to conventional margins) as the angular component is by far the largest contributor to the margin area. The statistical approach to margin calculation, in addition, offers the possibility for advanced online verification and updating of breathing variation as more data become available.

(Some figures in this article are in colour only in the electronic version)

4317

1. Introduction

Studies based on daily electronic portal imaging and repeated fluoroscopy or CT imaging show that margin reduction, to the level required for dose escalation, cannot accommodate the errors of treatment set-up and organ motion (Little *et al* 2003, Ten Haken *et al* 1997, Stroom and Heijmen 2002, Hugo *et al* 2007). To successfully create a meaningful margin reduction in the presence of organ motion, one therefore may have to turn to efficient gating of the treatment delivery and/or real-time tracking of the target position.

Motion-gating techniques minimize the range of target motion during irradiation by limiting the delivery to pre-defined periods (duty cycle). The duration of irradiation is usually arranged to be that with the least variation in target position and/or maximal sparing of the surrounding normal tissue. The more technologically advanced approach of tumour tracking is associated with the idea of online synchronization of the treatment delivery to the tumour motion either by closed-loop tracking (i.e. observing the tumour excursion in real-time) or by open-loop tracking (i.e. using prediction algorithms from a baseline position model). Although closed-loop tracking could in theory track an arbitrary trajectory given a margin for feedback lag, these methods still have one common difficulty, which is the presupposition that breathing is reproducible throughout the planning and delivery process of treatment.

Breathing motion is not a robust and 100% reproducible process (Gierga *et al* 2004). In addition, it is easily imagined that the patient, when positioned on the treatment couch, may breathe very differently from imaged for planning due to discomfort and/or anxiety (Shirato *et al* 2004) or other physiological reasons. The role of prediction algorithms to describe target motion has been discussed in this context (Sharp *et al* 2004, Vedam *et al* 2004) but it has not been proven that any prediction algorithm can be robust enough to account for this variability in breathing motion. Furthermore, the idea of performing 4D optimization has been suggested to compensate for organ motion (Trofimov *et al* 2004), which involves the use of modified pencil beam kernels or time-weighted influence matrices to compensate for organ motion. Such an approach will increase the modulation gradients within intensity-modulated beams if not actively restricted, and will therefore be potentially even more prone to the variations in breathing motion. Whatever method is ultimately used for compensating for organ motion, the *variation* of breathing motion is unlikely to disappear for a free-breathing patient and a small margin will always be needed to provide compensation, even if all other treatment uncertainties are ignored. This also applies to 3D conformal treatments.

The variation in the breathing cycle has been commented on before (Vedam *et al* 2004, Zhang *et al* 2004, Nehmeh *et al* 2004, Seppenwoolde *et al* 2002, Ruan *et al* 2008), but never has this irreproducibility been the main subject of investigation with the purpose of deducing and evaluating an appropriate margin size to account for tumour motion uncertainty. This new *margin model* concept (Coolens *et al* 2005) is designed to follow the tumour trajectory and statistically addresses variations in breathing motion, which occur both during and between fractions. The margin for set-up errors was not considered as the model provides a safety margin that follows the tumour path and effectively constitutes the ITV margin (ICRU-62), which needs to be added to the former to compose the PTV from a clinical target volume.

The aim of this paper is therefore

(1) to present the model for calculating a dynamic internal margin (DIM), based on the observed variation in the breathing cycle and
(2) to describe the usefulness of the model in providing clinically relevant margins which are robust against variations in motion-induced target displacements.
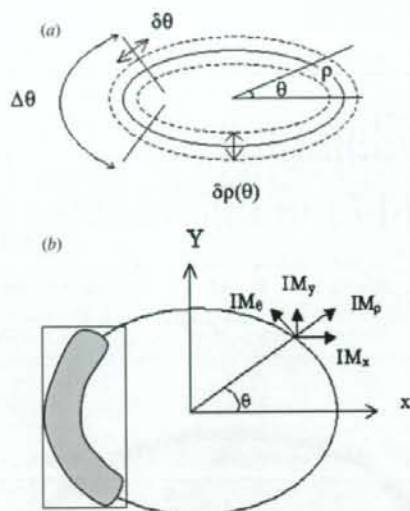
Figure 1. (a) Illustration of the several components that describe the variation in breathing-induced target position. The solid ellipse represents the average breathing motion with hysteresis (described by the polar angle, θ, and polar length, ρ). The two dotted ellipses represent the maximum deviation from this average. When gating the treatment, a gating window, $\Delta\theta$, will be used. For both tracking and gating there is an uncertainty in phase, $\delta\theta$, and a variation in target position per phase, $\delta\rho(\theta)$. (b) Illustration of the polar (i.e. along the curved trajectory) and Cartesian (i.e. rectangular) margin components and the influence on margin size.

2. Method

It has been shown that the respiration-induced motion of lung and liver tumours can display a strong hysteresis effect (Shirato *et al* 2004, Seppenwoolde *et al* 2001), i.e. the breathing forces governing inhalation and exhalation are different. As a consequence, the tumour displacements from inhale to exhale and vice versa do not follow the same path, which results in elliptically shaped tumour trajectories. It will be shown in this study that the hysteresis effect can be exploited to define ITV margins that follow the tumour trajectory and therefore minimize the amount of healthy tissue that otherwise would be irradiated. In addition, this approach allows compensating for the variation in breathing motion over time. An illustration of an elliptical motion trajectory subject to hysteresis is shown in figure 1. This figure will be used to describe the dynamic internal margin model (section 2.1). In the second part of the paper, the model will be applied to data of lung patients to (i) illustrate the effect on margin size and reduction in normal tissue irradiation and (ii) explain how such a dynamic margin model can work in practice for providing safe tumour tracking or gating in the presence of breathing variability.

2.1. Development of the DIM model

Considering the illustration in figure 1, if the patient would breathe perfectly reproducibly the target trajectory would follow an ellipse with zero width (the solid line). In practice though, one revolution following the path of the breathing cycle could take a variable time, depending
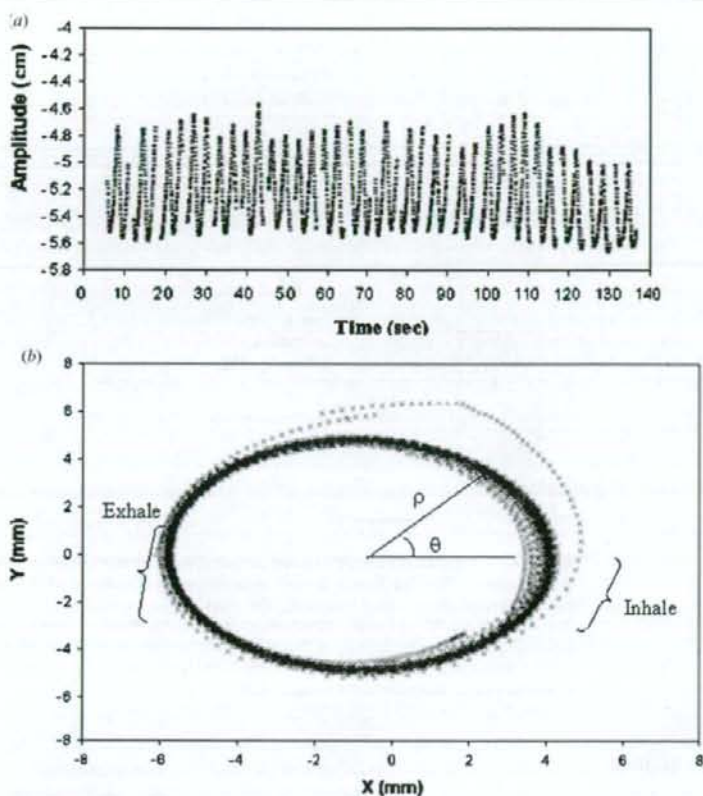
Figure 2. (a) Ant–Post displacement of a liver patient's diaphragm with time. (b) Representation of the data in a polar coordinate system by considering the amplitude as a 2D vector within a Cartesian coordinate system. The inhale phases correspond to the minimum amplitude points in (a). The polar coordinate system is described by the polar angle θ and polar length ρ (= amplitude).

on the period of the specific breathing cycle T. The variation in breathing period over time manifests itself in a certain width in motion amplitude with respiratory phase. This can be seen clearly in the patient data (figures 2 and 3) and has also previously been reported (Shirato *et al* 2004, Nehmeh *et al* 2004). The variation in the length of the semi-major and semi-minor axes of the elliptical trajectory shown in figure 1 indicates the 2D variation in target position due to breathing-induced organ motion. The area between the two dotted ellipses illustrates the motion limits that would contain the measured data points (e.g. 2 standard deviations) around the average breathing motion (solid ellipse). In the case where one is able to track or gate the target, this variation constitutes precisely the required internal margin (IM) for breathing variability. However, considering the limits in tracking accuracy, there will also be some phase uncertainty that has to be accounted for due to time lag and system response. The presented margin model described here treats all these variations statistically to provide confidence limits for variations in breathing from cycle-to-cycle and from fraction-to-fraction. The required measurements to derive the DIM margins for planning could be made at the time of simulation,
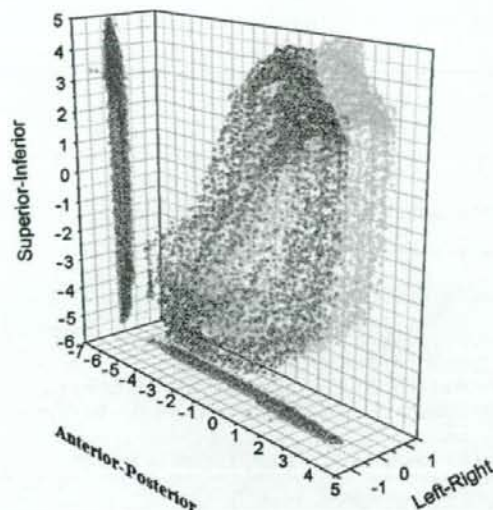
Figure 3. Lung tumour trajectory in 3D and projected onto the three main planes as acquired on day 1, referred to as session 1_1.

i.e. before treatment delivery (Gierga *et al* 2004, Vedam *et al* 2003, Ozhasoglu and Murphy 2002), and updated just before and/or during treatment as extra motion information becomes available.

2.1.1. DIM definitions. The various components involved in the DIM model are also indicated in figure 1. The range in target position at a certain phase θ is given by $\delta\rho(\theta)$ (where (θ) denotes a function of θ), which is twice the standard deviation, σ_ρ, from the average target position so as to give 95% confidence. To account for the fact that the breathing period is irregular (i.e. not constant), the reproducibility in arriving at the same phase as a function of time is defined as $\delta\theta$. This depends on the accuracy of the positional measurements as well as the stability of the breathing period. Similarly, this is determined as twice the standard deviation of the variation in phase angle with time, σ_θ. When gating treatment, the phase window, $\Delta\theta$, to which the treatment is confined, will describe a different variation in target position depending on what range of phases it encompasses. The latter is also referred to as the duty cycle, which is the fractional time of treatment for which the radiation is switched on. In summary, for *tracking* target motion, the envelope of the elliptical trajectories (call this the error or margin area) is therefore determined by $(\delta\rho, \delta\theta)$. When *gating* according to a certain duty cycle, the error area is determined by $(\delta\rho, \Delta\theta + \delta\theta)$. In the first instance the model was developed in 2D. An expansion to a 3D situation will be discussed later, but the only real difference this makes is the expansion from an error area to an error volume. Also an error area may be used in the plane of any treatment beam within good dosimetric accuracy.

2.1.2. DIM model. The model parametrizes both the radial and angular coordinates of tumour motion. The several components of the model (described in section 2.1.1) were designed to

split the angular uncertainty in two parts and therefore allow the margins to be shaped along the tumour trajectory. In the polar coordinate system with unit vectors $(\mathbf{e}_\rho, \mathbf{e}_\theta)$ the target position at a certain time t_0 can be written as a vector $\mathbf{r} = \rho \cdot \mathbf{e}_\rho$, with ρ the polar length (figure 1). For the situation here, the target positioning error, caused by a variation in motion amplitude $\delta\rho$ and uncertainty in phase, $\delta\theta$, is given by

$$\mathrm{d}\mathbf{r} = \delta\rho \cdot \mathbf{e}_\rho + \rho \cdot \delta\theta \cdot \mathbf{e}_\theta. \tag{1}$$

For gating, a phase-dependence must be included (depending on the gating window):

$$\Theta = \Delta\theta + \delta\theta. \tag{2}$$

The two parameters that define the error area thus are

$$\boxed{\mathrm{IM}_\rho = \delta\rho, \qquad \mathrm{IM}_\theta = \rho \cdot \Theta.} \tag{3}$$

It is possible to express these parameters in the Cartesian coordinates by projecting them onto the x- and y-axis. The 2D Cartesian components to the IM can then be written as

$$\boxed{\begin{aligned} \mathrm{IM}_x &= \delta\rho(\Theta) \cdot \cos\theta - \rho \cdot \Theta \cdot \sin\theta, \\ \mathrm{IM}_y &= \delta\rho(\Theta) \cdot \sin\theta + \rho \cdot \Theta \cdot \cos\theta. \end{aligned}} \tag{4}$$

Both the polar and Cartesian margin components are illustrated in figure 2(b).

2.2. Application to patient data

2.2.1. Abdominal motion. To illustrate the model characteristics, real, i.e. irregular, motion data are used. Figure 2(a) shows the anterior–posterior displacement of an infrared marker placed on the abdominal surface of a liver patient as detected by the RPM system (Varian, PA). This one-dimensional data can be transformed into a 2D beam's eye-view motion of a tumour by considering the Ant–Post amplitude displacement as a Cartesian vector and projecting it onto its orthogonal X- and Y-axes with phase ($X = A\cos\theta$, $Y = A\sin\theta$, with A the amplitude and θ the phase at that point). Although this is not a real internal tumour trajectory, it will be assumed to be one for the purpose of portraying the model characteristics in the presence of breathing irregularities and elliptical hysteresis. The positions of inhale and exhale are indicated in figure 2(b). The variation in breathing amplitude is clearly visible through the width of the ellipse-like trajectory. In addition, it can be seen that this width changes with phase due to variations in amplitude. This is important when gating treatment delivery to a certain phase window or duty cycle, as the margin may be phase dependent. Furthermore, a clear deviation from the average breathing trend can be seen in the upper right-hand corner of the plot. This large deviation could be due to a sudden change in breathing pattern, when the patient coughs, for example, or it could constitute the sampling of extremes of a stochastic distribution. This illustrates that having an unexpected change in breathing pattern would be, at best, very hard to account for with motion prediction models and be potentially dangerous to ignore in practice.

2.2.1.1. Variation in target position and respiratory cycle. To calculate the variation in target position at a certain respiratory phase, an ellipse was fitted to the data in figure 2(b) by performing a least-squares minimization of the five parameters that describe it. These parameters were semi-axes a and b, together with the coordinates (x_0, y_0) that describe the origin of the ellipse and a tilt in the ellipse's major and minor axes, ϕ, with respect to the

Cartesian coordinate system. The points on the fitted ellipse were transformed into x- and y-coordinates with the following transformation:

$$\begin{cases} x = x_0 + \cos\phi \cdot \dfrac{x'}{a} - \sin\phi \cdot \dfrac{y'}{b}, \\ y = y_0 + \sin\phi \cdot \dfrac{x'}{a} + \cos\phi \cdot \dfrac{y'}{b}. \end{cases} \tag{5}$$

The variation in motion amplitude, σ_ρ, can then be calculated as the difference between the amplitude at the measured data point (x_i, y_i) and the average amplitude at the point (x, y) with corresponding phase, as derived from the elliptical fit:

$$\sigma_\rho(\vartheta) = \sqrt{x_i^2 + y_i^2} - \sqrt{x^2 + y^2} \qquad \text{with} \qquad \frac{x}{y} = \frac{x_i}{y_i}. \tag{6}$$

The variation in respiratory cycle, i.e. the temporal variation in phase was analysed as follows. First, the running average breathing time, $T_{\text{av}, i}$, was determined as the average of the time between the phase midpoints (2π apart), over the last 'i' number of consecutive breathing cycles, i and, with n being the total number of cycles here equal to 25:

$$T_{\text{av}, i} = \sum_{k=1}^{i} \tau_i / n. \tag{7}$$

This is done to mimic the online tracking approach where all available data up and until that point are used. Then, the angular variation, σ_θ, i.e. the difference in phase at a certain time t and the time $t + T_{\text{av}, i}$, was calculated. For these data, there were 30 phase samples per second and a total study time of 196 s. The variation in respiratory cycle, as illustrated in figure 1, is then defined as

$$\delta\theta = 2\sigma_\theta \tag{8}$$

with the use of 2 standard deviations to give the 95% confidence limit.

2.2.1.2. Assessment of DIM margins versus conventional margins.

Making a comparison of the error area obtained from the polar and Cartesian margin components assessed the effect of using the dynamic margin approach. The components IM_x and IM_y were calculated from the previously obtained polar and angular margin components according to equation (4). The area covered by the margins is then given by $2IM_x \times 2IM_y$ (Cartesian) or $2IM_\rho \times 2IM_\theta$ (polar). As the dynamic margins are designed to follow the trajectory of motion, it would be expected that they reduce the amount of normal tissue irradiated compared to conventional margins that consider the maximum extent of motion. Note that this model addresses variations in breathing motion, which occur both during and between fractions. In practice, there will be two types of measurements related to motion. The first one involves fluoroscopy or cone beam CT (CBCT) to estimate the mean tumour position trajectory over time. The second component will address the variability of motion around this mean position to calculate the margin components, as described by the model.

2.2.2. Lung tumour internal trajectories.

Data for this part of the study consisted of real-time 3D lung tumour position coordinates from two patients on two treatment days. For ease of use, they will be further referred to as session 1_1 (day 1) and session 1_2 (day 2). Similarly, data for patient 2 will be referenced as session 2_1 (day 1) and session 2_2 (day 2). The target was represented by a single 2 mm gold marker that had been implanted in the tumour and was tracked over a period of up to 3.3 min under fluoroscopy at a frequency of 30 Hz (Seppenwoolde *et al* 2002, Shirato *et al* 2000). Figure 3 illustrates the tumour trajectory in session 1_1.

2.2.2.1. Lung tumour margins. Given the minimal variation in tumour position in the left–right (LR) direction for these particular patients, attention was focused in the first instance on the lateral beam's eye-view in which the more typical hysteresis is visible. Similarly to the margin derivation in section 2.2.1, the margins are derived by first obtaining the mean tumour trajectory, followed by calculating the 95% confidence levels around that mean. However, figure 5 illustrates that to find the mean tumour trajectory a more flexible fitting process might be needed than a purely elliptical path.

The mean trajectory was therefore estimated using a moving average calculation around the centre of mass of the entire data set. As the trajectory is a function of time or breathing phase, the data were sub-sampled in different breathing phases or time intervals. Within each sub-sample (i.e. data bin) a least-squares fit determined the mean positions. The number of sub-sample bins associated with the averaging was determined by balancing the smoothness of fit with the fit residual error.

To calculate the phase component of the margin, it was needed to compare individual phase points to the mean phase calculation. As described in section 2.2.1.1 a running average of the breathing period was calculated (see also equation (8)) to represent the average phase trajectory. The DIM components were then calculated as before through the statistical analysis of the breathing variation around the mean in both amplitude and phase. If there is little, or no, hysteresis, such as, e.g., in the LR direction in figure 3, then the DIM margins may still be along the main axis of motion, with the phase margin set equal to the width of the phase bin. This technique was applied if the range of motion in one direction was smaller than 1.5 mm (see discussion). This situation will be referred to further on in the results section as a 'low' hysteresis trajectory, as opposed to a 'high' hysteresis where the tumour clearly rotates round the centre-of-mass.

2.2.2.2. Margin robustness. To test the model robustness, the variation in tumour motion on day 2 was compared to that for day 1 by overlaying the mean tumour trajectories on top of each other with the associated DIM margins. The aim was to mimic a potential clinical implementation by which the margins and mean trajectory would be determined offline from, e.g., simulator fluoroscopy and/or 4DCT data. Then, the second trace was used as the 'treatment' trace for which an offline or online scenario would be possible. The offline approach could involve, e.g., set-up imaging with CBCT or planar kV in the required beam's eye-view to establish the mean trajectory is (a) still similar to the one used for planning and (b) assess and recalculate the margins on the day for comparison with the plan margins. In an online tracking protocol, it could be envisaged to have the system track and predict not only the tumour position but calculate the margins with increasingly higher statistical significance as data are being acquired.

3. Results

3.1. DIM model characteristics

To illustrate some of the model characteristics, the average target motion in figure 2(b) was estimated by fitting an ellipse to the data (optimal parameters: $a = 4.9$ mm, $b = 4.9$ mm, $x_0 = -0.3$ mm, $y_0 = -0.2$ mm and $\phi = -0.45$ rad). The combination of both polar and angular errors is plotted in figure 4 with the measured data points (only a subset of the points is shown for clarity). This shows the error area as a function of phase in the breathing cycle. As exhale has proven to be the most stable phase in the breathing cycle, the IM components have been calculated for a number of gating window sizes around this phase (table 1). As expected,
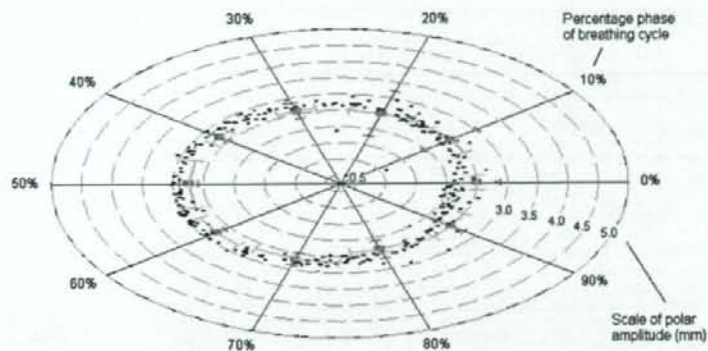
Figure 4. Plot showing the polar (pink) and angular (green) IM for the measured breathing motion (see figure 2) per percentage of the average breathing cycle. Only a subset of the points is shown, for clarity. The internal concentric circles represent the amplitude (of AP displacement) scale of 0.5 mm.

Table 1. Table demonstrating the differences in margin area and internal margins, in polar (IM_ρ) and angular (IM_θ) distance (equation (4)), for different duty cycles around the exhale phase for the data in figure 2(b).

Duty cycle (%)	0	20	30	40	50
IM_ρ (mm)	0.2	0.2	0.3	0.4	0.4
IM_θ (mm)	0.4	4.0	5.6	7.1	8.6
IM_x (mm)	0.4	2.5	3.5	4.4	5.4
IM_y (mm)	0.3	3.1	4.3	5.5	6.7
Polar area (mm^2)	0.3	3.2	6.0	9.9	13.4
Cartesian area (mm^2)	0.4	31.3	61.4	98.2	144.5

the margin size increases significantly with increasing duty cycle (Hugo *et al* 2002). The component in the angular direction is the most crucial contributor to the size of the margin. In addition, a comparison of the Cartesian and polar margin area is given. The error area covered by the polar margins is smaller than by the Cartesian components. This difference becomes even more prominent as the gating window size increases and indicates the benefits of using the DIM model in sparing normal tissues from high-dose irradiation.

3.2. Dynamic margins for lung tumour internal trajectories

3.2.1. High hysteresis. The lateral projections for all four sessions are shown in figure 5 together with the best-fit ellipse, the average trajectory and the bin-width from the centre-of-mass. In this case, however, the number of bins used to average the trajectory was determined by balancing the smoothness of fit with the fit residual error and was chosen to be equal to 40. This corresponds to almost 10 bins per second, given that the average breathing period was approximately 3.6 s (patient 1) and 3.8 s (patient 2).

The associated DIM margins for all four sessions are summarized in table 2 and were calculated on the full extent of the motion to illustrate the total range of motion. The DIM components for different sessions show good agreement, with the exception of the amplitude error in session 2.2. This discrepancy is due to the drift in the tumour trajectory over time. A comparison of the Cartesian and DIM margin sizes (using the margin components of the
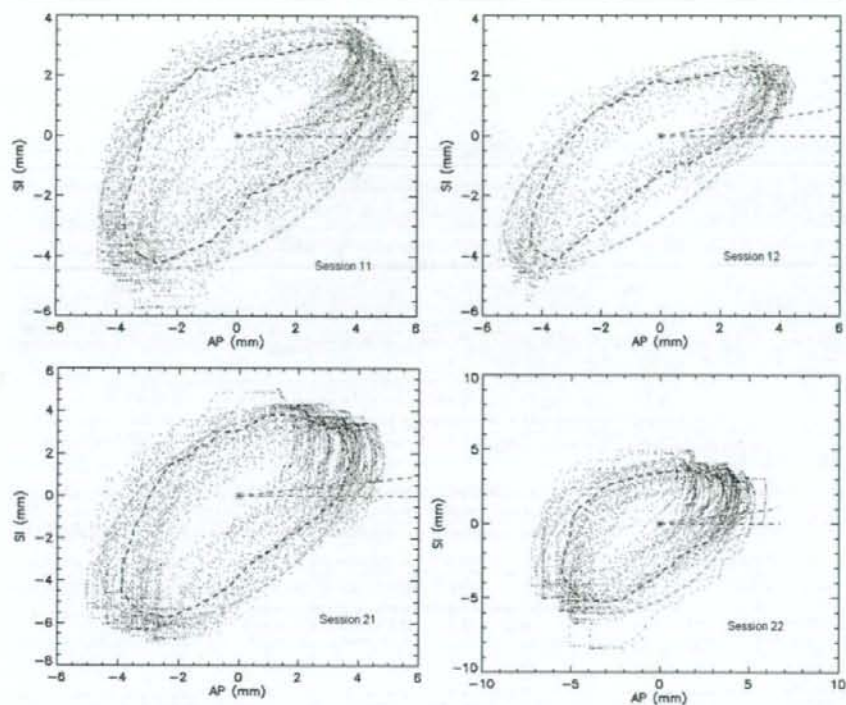
Figure 5. Lateral projection of tumour motion during all sessions. The (red) dotted line represents the average tumour trajectory calculated over a number of bins, the first of which is shown as radiating out from the centre-of-mass (in blue). The green/light grey line shows the best-fit ellipse to the data.

Table 2. Table listing the internal margins in both polar (IM_ρ) and angular (IM_θ) distance calculated over the entire lung tumour trajectory for the different data sessions, together with the polar and Cartesian error areas from these margins at the exhale phase (i.e. tracking of the target).

Session no	IM_ρ (mm)	IM_θ (mm)	Polar area (mm²)	Cartesian area (mm²)
1.1	1.8	2.0	14.4	12.6
1.2	1.7	2.0	13.6	12.3
2.1	1.8	2.0	13.6	12.3
2.2	2.4	1.9	18.2	12.3

entire trace but applied at exhale) is also given in table 2 and indicates (1) that in the case of tumour tracking, i.e. small margin values, the Cartesian margins are relatively insensitive to change in tumour amplitude and drifting of the tumour trajectory and (2) the margins are phase dependent as the variation in phase/amplitude at exhale is smaller than the total variation.

Table 3 lists the different margin components for a gated treatment with the impact of using different duty cycles. In this case, the reduction in margin area (and hence normal tissue irradiation) when using the polar margins is significant compared to the Cartesian standard margins.
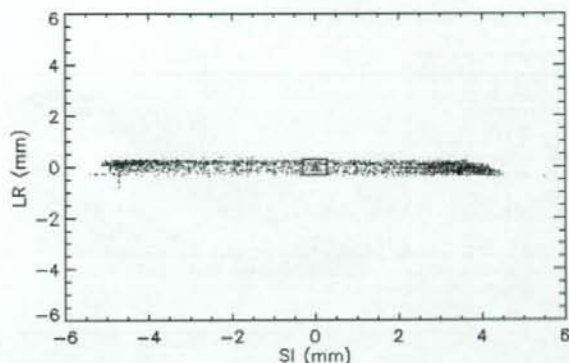
Figure 6. Anterior view of the tumour motion trajectory for session 1_1. The centre-of-mass is marked by a cross (in red). The margin area in that phase bin is indicated by the rectangle and would move along the SI axis with time between inhale and exhale.

Table 3. Table demonstrating the differences in margin area and internal margins, in polar (IM_ρ) and angular (IM_θ) distance (equation (4)), for different duty cycles around the exhale phase for session 1_1 in figure 5.

Duty cycle (%)	0	20	30	40	50
IM_ρ (mm)	1.6	1.7	1.7	1.8	1.8
IM_θ (mm)	2.0	4.0	5.3	6.7	9.2
IM_x (mm)	2.2	2.9	3.3	3.8	4.5
IM_y (mm)	1.4	3.2	4.5	5.8	8.2
Polar area (mm^2)	13.1	27.2	36.9	48.9	65.2
Cartesian area (mm^2)	12.2	36.9	59.3	87.5	147.2

3.2.2. Low hysteresis. The anterior BEV of session 1_1 is shown in figure 6 and displays a 'low' hysteresis trajectory. For this situation, the margins were calculated for ten phase bins (as per standard 4DCT). The amplitude margin was determined to be twice the standard deviation from the centre-of-mass for all data points in the LR direction, resulting in $IM_\rho = 0.35$ mm. The phase margin was calculated as before from the variation of the running time average and was, on average, equal to 2.2 mm. The resulting DIM margin area therefore was 1.5 mm^2 per phase bin for which the target would be irradiated.

3.2.3. Robustness. To assess the potential of applying the DIM margins from day 1 to account for the variability in breathing in further treatments, the full tumour trajectories of sessions 1_1 and 1_2 are overlaid in figure 7(a). It can be seen that the lung tumour motion follows a similar trajectory with time for both sessions. The DIM margins are shown in figure 7(b) as error bars on top of the average tumour trajectory and cover most of the breathing variability in session 1_2. The mean trajectories show very good similarity but, as discussed earlier, due to the drifting in session 2_2, the mean tumour path appears larger than in sessions 2_1 and potentially a little rotated as well. The drifting of the tumour trajectory with time can then also be a confounding factor in determining the required margins and this means that the 95% confidence levels were not sufficient to provide margins in the event of drifting. Note that the 99% confidence limits are only just covering the mean trajectory.
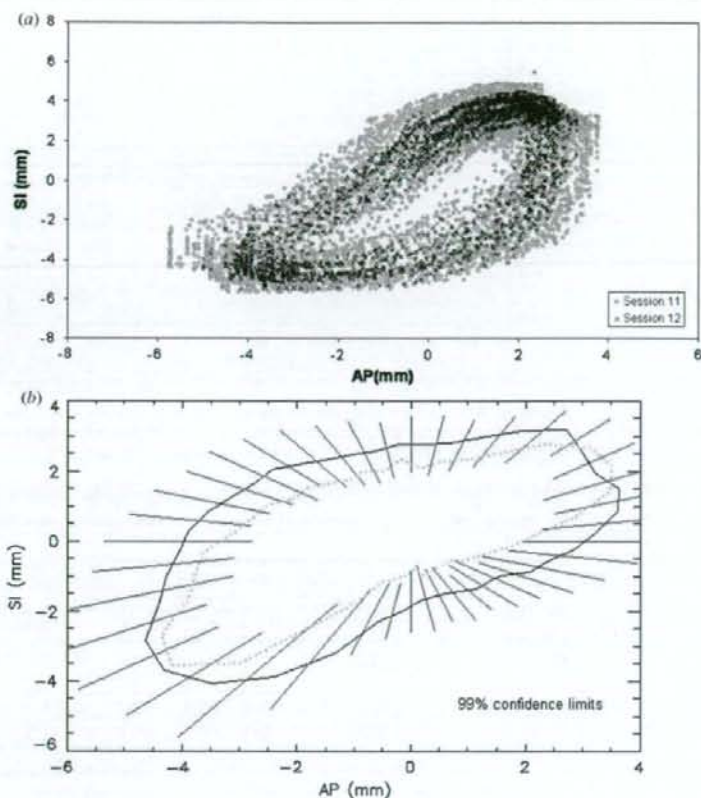
Figure 7. (a) Tumour trajectories in AP–SI view for patient 1. (b) Average tumour trajectories for this patient (session 1_1 as solid line; session 1_2 as dotted line) centred on the original COM coordinates with margin bars from session 1_1.

More advanced statistics and more representative samples of inter-fraction variability (as data become available) should improve this significantly.

4. Discussion

The DIM model was developed for tracking or gating of the treatment delivery, as it is convenient to have a margin that follows the tumour trajectory (i.e. lies along the gating window) so as to maximally spare normal tissues. The internal margin components were calculated in a polar coordinate system, allowing the motion margin to have an axis in the motion direction. The Cartesian components of the IM could be used but this will create a rectangular margin that will in general be larger than the corresponding polar segment. In the case of low or no hysteresis the differences between the Cartesian and DIM margins would be minimal, but applying margins that stretch along the line of motion will provide extra robustness and flexibility to account for potential changes during treatment and smaller margins. Once the statistical margins have been established from pre-planning measurements,

the model could be applied at the treatment stage to verify that the motion uncertainty lies within the planned margins. This could be done either just before beam-on or, in a more advanced situation, even during irradiation with real-time feedback. The flexibility of the DIM model means that data can be readily added as it becomes available during treatment to update the motion statistics and hence margins for an individual patient.

As yet the DIM model was developed in 2D. An extension of the DIM model to a 3D situation would be possible and would need the description of the model components in the general curvilinear coordinates (q_1, q_2, q_3) rather than the polar cylindrical coordinates (ρ, θ, z). The resulting error volume will resemble a (possibly deformed) torus. However, taking fluoroscopy measurements in two orthogonal fields of view could provide information for the incorporation of the third dimension. Figure 3 also indicates that it might not be needed to extend the model to 3D if, e.g., the LR motion is inherently small. In addition, the beam angles could be chosen so that their BEV projection minimizes the tumour motion.

The total number of phase bins (and hence the smallest phase bin size) would depend on the tracking system's feedback accuracy. Similarly, the cut-off value for when to decide on a 'low' or 'high' hysteresis approach will depend on the spatial accuracy of the tracking system as well as the size of the fiducial marker and tumour being tracked and the clinical relevance of such a displacement. Currently, the model can only be accurately applied when there is no drift present that extends beyond the centre-of-mass of the average trajectory. It seems unlikely that breathing coaching could counteract or help alleviate this problem but the drifting could also be incorporated into the DIM model, which will be the topic of further study through different statistics and modelling of the mean trajectory.

Despite the increasing knowledge about lung tumour motion, accurate data on 3D real-time tumour trajectories are still limited and mostly acquired through kV tracking. Practically, the implementation of a DIM model would require internal motion information (e.g. from fluoroscopy), at least until the relationship between internal and external motion can be quantified accurately (Ozhasoglu and Murphy 2002). Alternatively, electro-magnetic systems with implantable transponders hold promise to provide this real-time information (Schweikard et al 2000).

The irreproducibility of the breathing cycle is important not only for gating or tracking of the target but also when considering incorporating organ motion into leaf sequencing files. Some researchers have commented on this motion-compensation method with the aim of planning treatment on 4D CT data and creating a leaf segment database from which the MLC controller can pick a segment according to the phase of breathing (Vedam et al 2004, Keall 2004). Whether or not this is a technically feasible technique remains to be proven, but it certainly does emphasize the need for reproducible and accurate information on breathing-induced motion and appropriate margins, regardless of what motion compensation method is ultimately used.

5. Conclusion

Attention was turned in this paper to organ motion compensation methods such as gating of treatment delivery and tracking of target position. An issue that has mostly been ignored in the development of these techniques is the fact that breathing motion is not a perfectly reproducible process. The aim of this study was therefore to present a new model that calculates a dynamic internal motion margin, based on the observed variation in the breathing cycle and which minimizes the volume of normal tissue irradiated by shaping them along the tumour trajectory. It determines an error area in polar coordinates based on the hysteresis variation of the breathing cycle over time, i.e. the statistical uncertainty in motion amplitude

and phase reproducibility. This was then developed further for application to real lung tumour trajectories. It was shown that this model proved to be successful in reducing margins for lung tumour motion compared to conventional margins. The phases around exhale were found to have the smallest variation in both phase and amplitude. The phase component dominates the margin size and a larger margin would be needed if a gating window were used. It was shown that the model significantly reduces normal tissue irradiation in this situation and offers the possibility for advanced online verification of breathing motion.

Acknowledgment

References

Coolens C, Webb S and Evans P 2005 A dynamic margin model to account for organ motion variability *Rad. Oncol.* **76** (Suppl. 2) S183

Gierga D P *et al* 2004 Quantification of respiration-induced abdominal tumor motion and its impact on IMRT dose distributions *Int. J. Radiat. Oncol. Biol. Phys.* **58** 1584–95

Hugo G D, Agazaryan N and Solberg T D 2002 An evaluation of gating window size, delivery method, and composite field dosimetry of respiratory-gated IMRT *Med. Phys.* **29** 2517–25

Hugo G D, Yan D and Liang J 2007 Population and patient-specific target margins for 4D adaptive radiotherapy to account for intra- and inter-fraction variation in lung tumour position *Phys. Med. Biol.* **52** 257–74

Keall P J 2004 4-Dimensional computed tomography imaging and treatment planning *Semin. Radiat. Oncol.* **14** 81–90

Little D J, Dong L, Levy L B, Chandra A and Kuban D A 2003 Use of portal images and BAT ultrasonography to measure setup error and organ motion for prostate IMRT: implications for treatment margins *Int. J. Radiat. Oncol. Biol. Phys.* **56** 1218–24

Nehmeh S A *et al* 2004 Quantitation of respiratory motion during 4D-PET/CT acquisition *Med. Phys.* **31** 1333–8

Ozhasoglu C and Murphy M J 2002 Issues in respiratory motion compensation during external-beam radiotherapy *Int. J. Radiat. Oncol. Biol. Phys.* **52** 1389–99

Ruan D, Fessler J A and Balter J M 2008 Mean position tracking of respiratory motion *Med. Phys.* **35** 782–92

Schweikard A, Glosser G, Bodduluri M, Murphy M J and Adler J R 2000 Robotic motion compensation for respiratory movement during radiosurgery *Comput. Aided Surg.* **5** 263–77

Seppenwoolde Y *et al* 2001 3D tumor motion in lung due to breathing and heartbeat, measured during real-time tumor tracking radiation therapy *Int. J. Radiat. Oncol. Biol. Phys.* **51** 24

Seppenwoolde Y *et al* 2002 Precise and real-time measurement of 3D tumor motion in lung due to breathing and heartbeat, measured during radiotherapy *Int. J. Radiat. Oncol. Biol. Phys.* **53** 822–34

Sharp G C, Jiang S B, Shimizu S and Shirato H 2004 Prediction of respiratory tumour motion for real-time image-guided radiotherapy *Phys. Med. Biol.* **49** 425–40

Shirato H *et al* 2000 Physical aspects of a real-time tumor-tracking system for gated radiotherapy *Int. J. Radiat. Oncol. Biol. Phys.* **48** 1187–95

Shirato H, Seppenwoolde Y, Kitamura K, Onimura R and Shimizu S 2004 Intrafractional tumor motion: lung and liver *Semin. Radiat. Oncol.* **14** 10–8

Stroom J C and Heijmen B J 2002 Geometrical uncertainties, radiotherapy planning margins, and the ICRU-62 report *Radiother. Oncol.* **64** 75–83

Ten Haken R K, Balter J M, Marsh L H, Robertson J M and Lawrence T S 1997 Potential benefits of eliminating planning target volume expansions for patient breathing in the treatment of liver tumors *Int. J. Radiat. Oncol. Biol. Phys.* **38** 613–7

Trofimov A *et al* 2004 Development of tempero-spatial (4D) radiotherapy optimisation techniques *Med. Phys.* **31** 1776

Vedam S S *et al* 2003 Quantifying the predictability of diaphragm motion during respiration with a noninvasive external marker *Med. Phys.* **30** 505–13

Vedam S S *et al* 2004 Predicting respiratory motion for four-dimensional radiotherapy *Med. Phys.* **31** 2274–83

Zhang T *et al* 2004 Treatment plan optimization incorporating respiratory motion *Med. Phys.* **31** 1576–86

Postal dosimetry

Feasibility study of glass dosimeter postal dosimetry audit of high-energy radiotherapy photon beams

Hideyuki Mizuno[a,*], Tatsuaki Kanai[a], Yohsuke Kusano[b], Susumu Ko[a], Mari Ono[c],
Akifumi Fukumura[a], Kyoko Abe[d], Kanae Nishizawa[a], Munefumi Shimbo[e],
Suoh Sakata[f], Satoshi Ishikura[g], Hiroshi Ikeda[g]

[a]Research Center for Charged Particle Therapy, National Institute of Radiological Sciences, Chiba, Japan, [b]Accelerator Engineering
Corporation, Chiba, Japan, [c]Keio University Hospital, Tokyo, Japan, [d]Toho University Graduate School,
Funabashi, Japan, [e]Saitama Medical Center, Kawagoe, Japan, [f]Association for Nuclear Technology in Medicine,
Tokyo, Japan, [g]National Cancer Center, Tokyo, Japan

Author

Introduction: The characteristics of a glass dosimeter were investigated for its potential use as a tool for postal dose audits. Reproducibility, energy dependence, field size and depth dependence were compared to those of a thermoluminescence dosimeter (TLD), which has been the major tool for postal dose audits worldwide.

Materials and methods: A glass dosimeter, GD-302M (Asahi Techno Glass Co.) and a TLD, TLD-100 chip (Harshaw Co.) were irradiated with γ-rays from a ^{60}Co unit and X-rays from a medical linear accelerator (4, 6, 10 and 20 MV).

Results: The dosimetric characteristics of the glass dosimeter were almost equivalent to those of the TLD, in terms of utility for dosimetry under the reference condition, which is a 10×10 cm^2 field and 10 cm depth. Because of its reduced fading, compared to the TLD, and easy quality control with the ID number, the glass dosimeter proved to be a suitable tool for postal dose audits. Then, we conducted postal dose surveys of over 100 facilities and got good agreement, with a standard deviation of about 1.3%.

Conclusions: Based on this study, postal dose audits throughout Japan will be carried out using a glass dosimeter.
© 2007 Elsevier Ireland Ltd. All rights reserved. Radiotherapy and Oncology 86 (2008) 258–263.

Keywords: Postal dose audit; Glass dosimeter; Reference condition

---

Thermoluminescence dosimeters (TLD) have been used as the standard tool for dose audits for the past few decades [1,5,9,10]. They have good reproducibility and small energy dependence [12,13]. However, TLD powder requires careful handling and fading correction. On the other hand, glass dosimeters are almost free from the fading effect and can be read repeatedly [15]. They have been used for personal radiation monitoring for a long time. However, the problems of its high pre-dose and energy dependence prevented this tool from becoming an alternative to TLD [15]. Recently, a new type of glass rod dosimeter has become commercially available, which achieves great improvement in the reading method to avoid pre-dose effect [4]. Tsuda [17] reported its reproducibility as 0.82% in the coefficient of variance, which is comparable that of to TLD. Furthermore, good linearity, up to 10 Gy, and less fading, 1.90% after 129 days, were also achieved. Araki et al. [2] used a glass dosimeter to measure the Gamma-Knife helmet output factors and gave an indication of its superiority over TLD. They [3] also applied the glass dosimeter to linac beams of several energies and achieved slight energy dependencies

within 2%. The glass dosimeter's energy dependence is not a serious impediment to dosimetry under reference conditions.

Regarding the audit system, IAEA/WHO, the Radiological Physics Center (RPC) and the European Society for Therapeutic Radiology and Oncology (ESTRO) have performed postal dose audits worldwide or nationwide [1,5,6,9–11]. However, Japan has not yet been included in any audit group. In Japan, only a few pilot studies have been done [7]. Shimbo et al. [16] developed the postal dose audit system using a glass dosimeter. We are now on a project to establish a permanent dose audit system based on their system. Glass dosimeters have the potential to become the next generation of detectors for the audit system because of their handling advantage, reduced fading (relative to TLD) and repeatable readout. In this article, we report the comparison between a glass dosimeter and TLD as the tool for postal audits, focusing on its application to reference condition dosimetry. In addition, the results of the pilot postal audit study are shown, which was conducted at over 100 radiotherapy facilities.

Materials

Glass dosimeter

The glass dosimeter (DOSE ACE, Asahi Techno Glass Corporation; ATG) is silver-activated phosphate glass. Its weight composition is as follows: 11.0% Na, 31.55% P, 51.16% O, 6.12% Al and 0.17% Ag [17]. Though it is not the tissue-equivalent material, it does not affect our application such as relative dosimetry between our standard dose and the dose of certain hospital. Its dimensions are 1.5 mm in diameter and 12 mm in length. ID number is engraved for each element. It is based on radiophotoluminescence (RPL). Radiations produce RPL centers, which emit orange luminescence by UV-ray excitation. After emitting the luminescence, they will return to the stable RPL centers. Therefore, the numbers of RPL centers stay constant, allowing infinite numbers of readings for the same irradiation. In this study, outputs of glass dosimeters were average of five times sequential reading. The RPL centers are cleared by annealing (400 °C with 30 min), so that we can use the element sequentially. An FDG-1000 (ATG) was used as a reader.

The major dosimetric features taken into account were reproducibility and energy dependence. The reproducibility of the RPL signal depends on the element's cutting precision and UV-ray output stability. As for energy dependence, the mass energy absorption coefficient of the glass dosimeter, silver-activated metaphosphate, is several times higher than that of TLD, LiF, for low energy photons around 25 keV (see Fig. 1). This can affect the energy dependence factor.

Thermoluminescent dosimeter

The thermoluminescent dosimeter (TLD-100, Harshaw) is lithium fluoride doped with magnesium and titanium. Several forms are provided such as powders, chips, rods and cubes. Absorbed energy is stored in the crystal lattice, which results in visible light emission by heating. Because of its good physical aspects, including size, tissue-equivalent composition and fine reproducibility, the TLD-100 has been widely used as a postal dose audit tool. We used a chip type with a size of 3.2 mm × 3.2 mm × 0.9 mm. The reader was a Harshaw 5500. The reading temperature is from 50 to 400 °C in order to accumulate the main peak (~210 °C)

of glow curve. Annealing was done by the combination of 400 °C for 1 h and 100 °C for 2 h.

Tough water phantom

A water equivalent solid phantom, called the tough water phantom (Kyoto Kagaku Co.), was used. It consists mainly of C, O and H. Its density, mean atomic number and electron density are 1.01 g/cm^3, 7.42 and 3.25 × 10^{23}/cm^3, respectively. Those of water are 1.00 g/cm^3, 7.42 and 3.34 × 10^{23}/cm^3, respectively. Its size was 30 cm × 30 cm, it was a slab type and its central region was gouged to contain the glass dosimeters and TLDs.

Investigation of dosimetric characteristics
Experiments

Reproducibility

Reproducibility was examined for both dosimeters, glass dosimeter and TLD, using ^{60}Co γ-rays (Yoshizawa-LA, TYC-3001) and linac X-rays (Varian, Clinac21EX; 6 MV, 10 MV). Dosimeters were set at a reference depth of 10 cm in the tough water phantom (Fig. 2). Field size was 16 cm ϕ for ^{60}Co γ-rays and 10 × 10 cm^2 for X-rays. For each beam, 15 elements were irradiated uniformly. Each element's output was corrected with its own sensitivity. Corrected outputs were divided by the average of 15 elements' output. The measurement cycle, from irradiation to annealing, was done three times to decrease the statistical error.

Energy dependence of glass dosimeter

Energy dependence was examined for the glass dosimeter using ^{60}Co γ-rays and linac X-rays (Mitsubishi, EXL-15DP; 4 MV, Varian, Clinac21EX; 6 MV, 10 MV and Clinac23EX; 20 MV). The experimental setup was the same as in Fig. 2, and the measurements using the ionization chamber were taken under the same conditions. The stability of the output of ^{60}Co γ-rays or linac X-rays was much less than 1%. Measurements were done several times to decrease the statistical error. For each measurement, at least 10 elements were used for one energy.
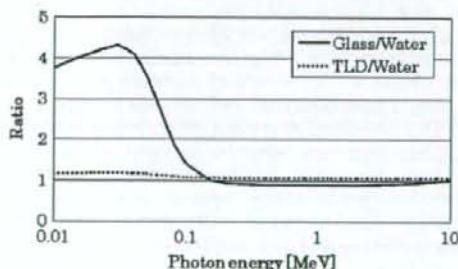

Fig. 1. The ratio of mass energy absorption coefficient between glass dosimeter (silver-activated metaphosphate)/TLD (LiF) and water (acquired from NIST database [14]).
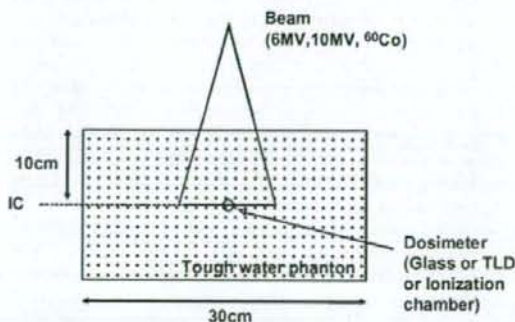

Fig. 2. Setup of reproducibility and energy dependence experiments; dosimeters were placed at 10 cm depth in the isocenter (IC).

The protocol used to determine the absolute dose was the Japanese code, Standard Dosimetry of Absorbed Dose in External Beam Radiotherapy (Standard Dosimetry 01), which is based mainly on IAEA Technical Reports Series No. 398.

Field size and depth dependence

To examine the glass dosimeter's response to low energy photons, field size and depth were changed, because the mean beam energy fell with increasing field size and decreasing depth. Both dosimeters, glass dosimeter and TLD, were irradiated using linac X-rays (Varian, Clinac21EX; 6 MV, 10 MV). Measurements were done at 5×5, 10×10 and 20×20 cm² field sizes and at the D_{max} (1.5 cm for 6 MV and 2.5 cm for 10 MV), 5, 10 and 20 cm depth in the tough water phantom. For each condition, 5 elements of glass dosimeter and 3 elements of TLD were used. Once again, the measurements using the ionization chamber were also done under the same condition, that is, measured in tough water phantom.

Results and discussion

Reproducibility

The deviations obtained from both the TLD and the glass dosimeter are shown in Fig. 3. The standard deviation was 0.8% for the glass dosimeter. This value is comparable to the TLD value, 0.7%.

Energy dependence of glass dosimeter

The obtained energy correction factor is shown in Table 1. They were represented as

$$E_q = \frac{Glass(Co)/D_{med}(Co)}{Glass(q)/D_{med}(q)}$$

where $Glass(Co)/D_{med}(Co)$ is the light output per unit dose in a medium for ⁶⁰Co γ-rays. $Glass(q)/D_{med}(q)$ is the light output per unit dose in the same medium for the beam quality q of interest. Beam quality q is represented as $TPR_{20,10}$. The glass dosimeter had a slightly positive correlation with beam energy. However, for the mega-voltage region, the
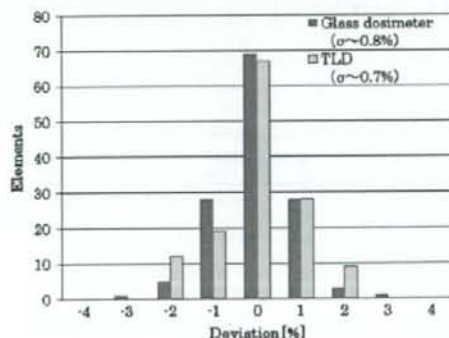
Table 1
Quality dependence of glass dosimeter in photon beams by experiment

Energy (MV)	$TPR_{20,10}$	Glass dosimeter factor (E_q)	TLD factor (IPSM 1990, [7,10])
⁶⁰Co γ-rays	0.58	1.000	1.000
4	0.624	1.007 ± 0.005	
6	0.669	1.014 ± 0.009	1.011
10	0.740	1.026 ± 0.007	1.023
20	0.791	1.029 ± 0.004	

levels of dependence were equivalent to those of the TLD achieved by IPSM [8,13] within the experimental errors. Their TLD factor was obtained by exchanging the glass dosimeter output to the TLD output of above equation.

Field size and depth dependence

The obtained ratios of readings from the glass dosimeter/TLD to ionization chamber outputs are shown in Fig. 4. The values were normalized at reference conditions, 10×10 cm² field and 10 cm depth. The ratios for the glass dosimeter were from 0.975 to 1.011 (mean 0.995) for 6 MV, and from 0.973 to 1.031 (mean 0.999) for 10 MV. Those for TLD were from 0.971 to 1.018 (mean 0.996) for 6 MV and from 0.985 to 1.038 (mean 1.014) for 10 MV.

The outputs of the glass dosimeter became slightly smaller, from 1.7 to 2.7%, for a 5×5 cm² field compared to 10×10 cm² and 20×20 cm² fields. This might have been caused by the change in energy spectrum. The mean energy of X-rays becomes higher in the smaller field because of the decrease in scattered photons within the field. However, overall, it seems that the ratios of the glass dosimeter were almost at the same level, or were rather stable, compared to the TLD, for changes in both field size and depth.

Discussion for the dosimetric properties

Even for non-reference dosimetry, glass dosimeter proved to be a potential alternative to TLD. Moreover, the glass dosimeter has the advantage of less fading. In the postal dose audit process, control elements are used to calibrate the reader. Known doses are irradiated onto the control elements by the audit director. Some audit groups irradiate the control elements at only the same timing as the intended facility's irradiation, to minimize the fading effect. By using glass dosimeter, this kind of limitation regarding fading becomes more flexible.

Postal dose audit trial

We conducted a pilot postal audit at over 100 radiation therapy facilities to verify the overall feasibility of establishing a postal dose audit system using glass dosimeters.

Postal tools

We sent 20 glass elements and one set of solid phantoms to participating facilities. The glass dosimeters were contained in tough water phantom (Fig. 5).

Fig. 3. Reproducibility of glass dosimeter and TLD; 45 elements were repeatedly irradiated by ⁶⁰Co, 6 and 10 MV X-rays.
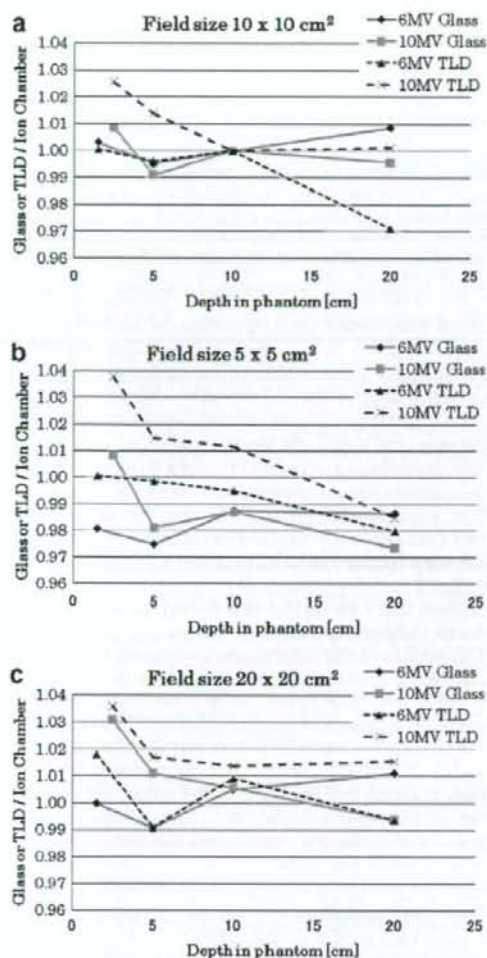
Fig. 4. Ratios between glass dosimeter/TLD and ionization chamber outputs for different field sizes and depths. The field sizes were (a) $10 \times 10 \, cm^2$, (b) $5 \times 5 \, cm^2$, (c) $20 \times 20 \, cm^2$, respectively. The values were normalized at reference conditions, $10 \times 10 \, cm^2$ field and 10 cm depth. The uncertainties of each measured value were 1.5% in standard deviation for glass dosimeter and 1.6% for TLD.

The assignments for the 20 glass elements are shown in Table 2. Twelve elements were "audit elements" that were irradiated with X-rays by a participant (six elements for each of two X-ray energies), six elements were "control elements" that were irradiated with a ^{60}Co beam at NIRS, and two elements were "background elements" that were not irradiated during the audit process. "Control elements" were used to calibrate the reader's sensitivity. These assignments were adopted to minimize the statistical error in final reading outputs under the limitation of the number of sequential readings, 20 elements for one reading run.
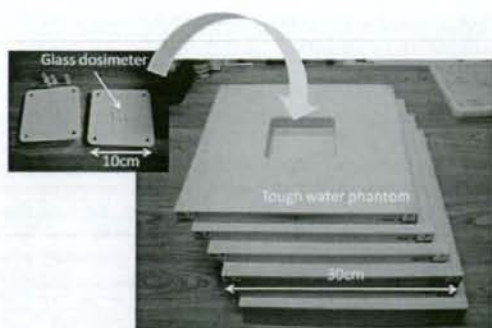

Fig. 5. Glass dosimeter and tough water phantom; tough water phantom is gouged to contain the glass dosimeters.

Table 2
Assignment of one set of glass dosimeters (20 elements)

Name	Element ID	Irradiation condition
Audit elements	Nos. 1–6	1 Gy is irradiated by applied facility by energy 1
	Nos. 7–12	1 Gy is irradiated by applied facility by energy 2
Control elements	Nos. 13–18	1 Gy is irradiated by NIRS by ^{60}Co
Background elements	Nos. 19 & 20	No irradiation

Determination of absorbed dose

The method this audit used to derive the output of irradiation dose to the glass dosimeters is shown below.

1. Twenty elements were read (one run).
2. We repeated the run five times. The rotation or position shifts of the element set in the reader were checked before each run.
3. Outputs of five runs were averaged for each element.
4. We multiplied by the following correction factors (definitions are shown later)
   - Elements' sensitivity correction factor
   - Energy correction factor
   - Phantom correction factor.
5. We averaged the six elements irradiated at the same energy.
6. We determined the calibration ratio between the output of the glass dosimeter and the ionization chamber from the ^{60}Co irradiated data.
7. We multiplied the calibration ratio by the audited elements' output.

The applied facility's final output was defined as in the following equation.

$$D = \sum_{i=1}^{6}(X_i \times I_i) \times E_q \times P_q \times \frac{Dose_{60Co}}{\sum_{i=13}^{18}(X_i \times I_i)}$$
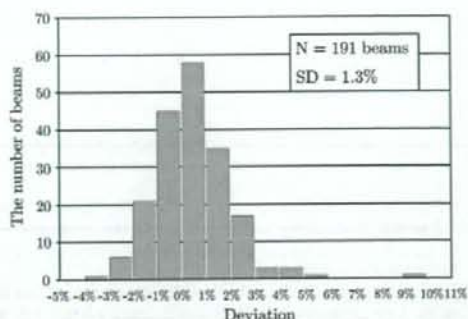
Fig. 6. The result of the postal dose audit for the 191 beams from 4 to 20 MV.

Table 3
Results of first and second postal dose audits

Facility	Beam quality (MV)	Deviation of audit		Probable causes
		First (%)	Second (%)	
A	4	4.1	1.9	Miscalculation of monitor unit
	10	9.2	0.9	(excluded daily MU calibration factor)
B	4	5.7	2.8	Mistake in measurement setup
	10	4.7	3.4	Mistake in calibration factor Substantial change in barometric pressure Uncalibrated thermobarometer
C	4	4.6	2.0	Unclear
	6	2.6	2.1	(Energy switching operation error?)

X_i is the raw output value of the glass element whose ID number is i, I_i is sensitivity correction factor of the glass element whose ID number is i (derived by uniform irradiation using ^{60}Co γ-rays).

$$I_i = \frac{D_{60_{Co}}}{X_i}$$

E_q is the energy correction factor of beam quality "q" (glass elements were irradiated by ^{60}Co γ-rays and 4, 6 and 10 MV X-rays. Correction factor was derived by using the output of the ionization chamber (IC), $D(^{60}\text{Co})$ and $D(q)$, which were measured at the same setup as the glass dosimeter).

$$E_q = \left[\frac{\sum_i X_i(^{60}\text{Co}) \times I_i}{\sum_i X_i(q) \times I_i} \right]^{\text{Glass}} \times \left[\frac{D(q)}{D(^{60}\text{Co})} \right]^{\text{IC}}$$

P_q is the phantom correction factor of beam quality "q."

$$P_q = \frac{D_w}{D_T}$$

D_w is the output of the ionization chamber irradiated by X-rays of beam quality "q" in 10 cm deep water, D_T is the output of the ionization chamber irradiated by X-rays of beam quality "q" 10 cm deep in the tough water phantom, $\text{Dose}_{60_{Co}}$ is the output of the ionization chamber irradiated by ^{60}Co γ-rays just before the irradiation of control elements (ID Nos. 13–18) with same setup.

I_i was assigned to each element to increase the outputs' precision. Of course, I_i, E_q and P_q were determined before the audit trial started. Accumulated uncertainty of each parameter was estimated to be 1.6% in one standard deviation.

Results of postal dose audit trial

We conducted the postal dose audit at 106 facilities using 191 beams. Seventy-seven beams were 4 MV, 31 beams were 6 MV, 81 beams were 10 MV, 1 beam was 14 MV and 1 beam was 20 MV. Fig. 6 shows the overall results of the outputs. The central value was 0.3% and standard deviation was 1.3%; 182 beams (95%) were within ±3%.

One facility showed a big deviation of over 9%. A second postal audit was conducted there, followed by an immediate hearing by phone. Finally, the apparent discrepancy was proved to arise from a participant's miscalculation of a monitor unit (excluding the correction factor of daily monitor chamber response). The result of the second postal audit at that facility was within 2%. Two other facilities, which showed deviations of more than 4%, also underwent a second postal audit. Those results are illustrated in Table 3. Clearly, the results were improved by the second audit, which showed the importance of external audits.

According to the ESTRO/EQUAL postal audit system [5], the optimum level is within ±3%, tolerance level is within ±5% and emergency level is over ±10% deviation. We followed these criteria to report the results to each facility. From this point of view, the reference dose is properly managed by these participants. In addition, glass dosimeters proved to be a suitable tool for postal dose audits.

Conclusion

The dosimetric features of glass dosimeters were examined and compared to those of TLD as tools for postal dose audits. Reproducibility and energy dependence were the same as in the TLD. Additionally, field size and depth dependence were at the same level, and were rather stable. Regarding handling advantages, repeatable readings and low fading, the glass dosimeter is likely to be a suitable tool for postal dose audits. Based on these results, and to check the overall system, we conducted a pilot postal audit at radiotherapy facilities. We got excellent results, in that the central value of the deviation was 0.3% and the standard deviation was 1.3%. A permanent postal dose audit system using glass dosimeters is therefore about to begin in Japan.